A Fast-Acting Method for Simulating Precipitation during Heat Treatment of Superalloy 718

S.L. Semiatin[1,*], J.S. Tiley[1], F. Zhang[2], T.M. Smith[3],
R.Y. Zhang[4], H.B. Dong[5], P. Gadaud[6], and J. Cormier[6]

[1] Air Force Research Laboratory, Materials and Manufacturing Directorate,
Wright-Patterson Air Force Base, OH 45433 USA
[2] CompuTherm LLC, Middleton, WI 53562 USA
[3] NASA Glenn Research Center, Cleveland, OH 44135 USA
[4] The Open University, Milton Keynes MK7 6AA, UK
[5] University of Leicester, Leicester LE1 7RH, UK
[6] Institut Pprime, UPR CNRS 3346, ISAE-ENSMA, 1 avenue Clément Ader,
BP 40109, 86961 Futuroscope-Chasseneuil Cedex, France
* Corresponding Author: sheldon.semiatin.1@us.af.mil

ABSTRACT

A fast-acting, mean-field method for simulating precipitation of the γ'' and γ' phases during aging of superalloy 718 following super-δ-solvus solution treatment was formulated and validated using observations in the literature. The approach assumed classical (homogeneous) nucleation and diffusion-controlled growth (N&G) of disk/ellipsoidal-shaped-γ'' and spherical-γ' particles. For the γ'' precipitates in particular, the evolution equations for both nucleation and growth incorporated corrections for the non-spherical shape, assuming a fixed aspect ratio. In addition, special attention was paid to the choice of input material properties for simulations. These parameters included the bulk free energies of transformation, particle-matrix (misfit) elastic strain energy (for γ''), effective diffusivities, and the γ''-γ and γ'-γ interface energies. The applicability of the diffusivities and interface energies chosen for the N&G simulations was established by their consistency in replicating previously-measured rate constants for the diffusion-controlled coarsening of both γ'' and γ'. The N&G formulation was discretized to obtain numerical (spreadsheet) solutions via the

Kampmann-Wagner approach. Simulation results for the temporal evolution of volume fraction and average size of the precipitates showed good agreement with experimental measurements. The sensitivity of model predictions to various input parameters was also quantified.

Key words: Superalloy 718, precipitation, nucleation and growth, coarsening, fast-acting simulation.

I. INTRODUCTION

Nickel-base superalloys are enabling materials for a variety of demanding high-temperature, load-bearing applications. These include service in both aerospace (propulsion) and land-base (power-generation) gas-turbine systems [1]. The importance of superalloys is underscored by long-running, quadrennial symposia (and state-of the art reviews therein) dedicated to superalloys in general and superalloys 718, 625, and 706 in particular, e.g. References 2-5.

Typically, components made from supealloys must withstand temperatures in the range between ~900 and 1400 K. In general, as the service temperature increases, the quantity of alloying elements in the superalloy (and concomitant volume fraction of ordered strengthening phase(s) such as fcc-like γ' (with an $L1_2$ structure) or bct γ'' (DO_{22}) precipitated in an fcc γ matrix) increases as well. Such variations in alloying content often dictate the type of material-synthesis approach. For superalloys that contain relatively-low or moderate amounts of alloying, synthesis usually comprises the casting of large ingots which are subsequently homogenized, hot worked to produce a recrystallized, moderately-fine grain size, and, finally, solution treated and aged. Materials in

this class include 718, 625, and Waspaloy. As alloy content (and the tendency for macrosegregation during melting and solidification) increases, fabrication methods based on melting, powder atomization, consolidation, hot working, and final heat treatment must be utilized. Powder metallurgy (PM) alloys made by this means include IN-100, Rene 88DT, and RR1000. Last, superalloys designed for the highest-temperature applications (e.g., Rene N5, PWA1484, CMSX-4 for turbine-blade applications) which often incorporate high levels of refractory elements are manufactured via directional-solidification (DS) techniques (e.g., the Bridgman or liquid-metal-cooling processes) to produce a single crystal or columnar DS grain structure.

The final heat treatment of superalloy components often consists of solution treatment and aging. For cast-and-wrought (ingot-metallurgy) parts such as those made from 718, solution treatment is followed by oil or water quenching and a single or two-step aging process to develop fine precipitate structures. By contrast, the more-highly-enriched PM superalloys are usually solution treated and cooled carefully (often to avoid quench cracking if the γ grain size is moderately-coarse) during which precipitation occurs simultaneously; this is followed by a final isothermal aging step to produce additional very fine precipitates. Selection of solution treatment temperature and aging temperature(s)/time(s) can be quite complex especially for materials such as 718 which contain both a grain-size-control phase (δ) and two strengthening phases (γ'' and γ').

The effect of heat-treatment parameters such as time and temperature (for isothermal treatments) or cooling rate on precipitation kinetics are often quantified by one of two broad types of techniques, i.e., empirical- (phenomenological-) or mechanism- based approaches. The former includes series of often-time-consuming heat treatments followed by metallography, hardness measurements, etc to assess the rate of approach to the equilibrium volume fraction and nominal size of precipitates during aging. The observations are then typically expressed in the form of isothermal-transformation (IT) or cooling-transformation (CT) diagrams. For 718, there have been numerous such measurements of IT and CT behavior [6-12]. Unfortunately, these measurements have often appeared to be contradictory, partly because of the difficulty of quantifying the early-stage nucleation and growth of very fine (nanometer-scale) γ'' and γ' phases as well as the effect of relatively-small variations in alloy content on phase equilibria and precipitation kinetics [13, 14].

Attempts to understand the nature of precipitation in superalloys more completely have relied on modeling-and-simulation methods that treat the detailed mechanisms and interplay of nucleation and growth (N&G) and sometimes coarsening. These methods fall into two broad categories, mean field and phase field. In the mean-field approach, standard relations for N&G [15] are utilized to describe the evolution of intragranular precipitates assuming a uniform (average) matrix composition (i.e., “mean field”) that provides the supersaturation driving force for such phenomena. The approach has been demonstrated to be especially useful for describing precipitation in γ'-strengthened PM superalloys [16-

[23]. Phase-field methods, on the other hand, can provide more-detailed information on the local evolution of concentration fields that control N&G. They have been utilized to investigate both isothermal and continuous-cooling heat treatments and have thus also been applied to provide insight into precipitation in γ-γ' nickel-base superalloys [24-26]. However, the technique is computationally complex and does not lend itself readily to the rapid evaluation of the effect of variations in heat treatment parameters, material composition/properties, etc. on microstructure prediction.

Compared to the numerous modeling efforts devoted to PM γ'-strengthened superalloys and selected other superalloys (e.g., 625 [27] and ATI 718Plus™ [28]), the simulation of aging heat treatments for cast-and-wrought 718 has received relatively-little attention [29-32]. Such limited work may be ascribed to challenges associated with the complex nature of the phase equilibria between the γ matrix, γ'' and γ' precipitates, and δ phase (at high temperatures) and the scarcity of kinetic data (i.e., diffusivities/mobilities) and other important input material properties (e.g., interface energies, bulk free energies of formation) required for such simulations. Because of such complexity, attempts to develop models for 718 have typically relied on commercial software packages such as PanPrecipitation™ and MatCalc™. In view of the current status related to 718, the current work was undertaken. Its objectives were threefold: (i) develop a fast-acting simulation method to describe the concurrent N&G of γ'' and γ' precipitates in 718, (ii) apply engineering-oriented methods to evaluate/obtain input material properties for the simulations, and (iii) validate the approach using prior

121 measurements in the literature and establish the sensitivity of predictions to the
122 input material properties. The work conducted to meet the objectives is
123 summarized in the following three sections on model formulation, input
124 properties, and validation/sensitivity analysis.

125 **II. MODEL FORMULATION**

126 A model was formulated to treat the concurrent nucleation and growth of
127 intragranular γ'' and γ' precipitates in superalloy 718. By and large, it was based
128 on classical expressions for homogeneous nucleation and diffusional growth,
129 taking into account the approximate shapes of the precipitates, i.e., disk/oblate
130 ellipsoid for γ'' and spherical for γ'. Specifically, γ'' precipitates were assumed to
131 have a diameter/major axis of length $L = 2r_{\gamma''}$, thickness/height of $e = 2h_{\gamma''}$, and
132 aspect ratio $q = e/L = h_{\gamma''}/r_{\gamma''}$. The radius of the γ' precipitates was denoted as $r_{\gamma'}$.
133 Expressions for precipitate coarsening incorporating shape effects were also
134 used. The key relations describing each phenomenon are summarized below.

135 A. *Nucleation*

136 The rate of precipitate nucleation, J, was described per the following
137 relation [15, 33, 34]:

138 $$J = \frac{2CDK_{\beta*}K_z}{a_o^4}\sqrt{\frac{\sigma}{k_BT}}\cdot\exp\left(-\frac{4\pi\sigma r^{*2}K_{\Delta G^*}}{3k_BT}\right)\cdot\exp(-\tau/t) = J_O\exp(-\tau/t)\,. \qquad (1)$$

139 Here, C and D are the atomic fraction of solute and solute diffusivity in the (γ)
140 matrix, a_O is the average lattice parameter of the matrix and precipitate phases
141 (taken here to be 0.37 nm), σ is the matrix-precipitate interface energy, k_B is
142 Boltzmann's constant (1.3806 JK^{-1}), T is the absolute temperature, and t is time.

For the disk-shaped γ'' with its anisotropic surface energy (due primarily to the tetragonality along the c axis), σ pertains to that for the l*ateral* (peripheral) γ''-γ interfaces. For the spherical γ' precipitates, σ is taken to be constant over the entire surface.

The critical radius of the precipitate, r*, depends on σ, the (chemical) free energy of transformation ΔG^* (taken as a positive quantity), and the elastic strain energy ΔG_{el} associated with the difference in lattice parameters of the matrix and precipitate phases (taken as a negative quantity), i.e.,

$$r^* = \frac{2\sigma}{\Delta G^* + \Delta G_{el}}, \qquad (2)$$

in which σ for γ'' pertains to the energy along the lateral interface as before. The elastic strain energy (per unit volume of precipitate) ΔG_{el} for γ'' formation was estimated from the classic expression derived by Christian [35]:

$$\Delta G_{el} = \frac{\mu}{(1-\upsilon)}\left\{\frac{2(1+\upsilon)\Delta^2}{9} + \frac{\pi q \delta^2}{4} + \frac{\pi q (1+\upsilon)\Delta\delta}{3}\right\} \qquad (3)$$

In Equation (3), μ and υ denote the average shear modulus and Poisson's ratio of the matrix and precipitate, Δ is an assumed uniform dilation and δ is the tetragonal distortion along the c axis ($\equiv \varepsilon_{33}^{T}$, the stress-free misfit strain along the c axis, minus $\Delta/3$) .

The constants K_{β^*}, K_Z, and $K_{\Delta G^*}$ in Equation (1) represent the ratios of the frequency factor, Zeldovich non-equilibrium factor, and ΔG^* for specific non-spherical nuclei relative to that for a spherical nucleus. For a cylindrical, disk-

shaped nucleus with an aspect ratio q (such as that formed by γ''), for example, these constants are as follows [36]:

$$K_{\beta^*} = 0.5\,(2q+1) \tag{4a}$$

$$K_Z = 2/\sqrt{6q}\,) \tag{4b}$$

$$K_{\Delta G^*} = 1.5q \tag{4c}$$

Similarly, if the γ'' precipitates are considered to have an oblate shape formed by rotating an ellipse about its minor axis and having a ratio of the lengths of the minor axis to major axis of q, the analogous expressions are [36]:

$$K_{\beta^*} = 0.5\,(1 + 2q - q^2) \tag{5a}$$

$$K_Z = \sqrt{\frac{2}{q(3-q^2)}} \tag{5b}$$

$$K_{\Delta G^*} = 0.5\,q\,(3-q^2) \tag{5c}$$

Values of K_{β^*}, K_Z, and $K_{\Delta G^*}$ for two values of q (0.5 and 0.333) are compared in Table I. The results indicate that similar values of $K_{\Delta G^*}$ and the product $K_{\beta^*} \times K_Z$ are obtained for a given q irrespective of whether the γ'' precipitate is modeled as a disk or oblate ellipsoid. In addition, an inspection of Equation (1) reveals that

Table I. Nucleation Rate Factors for Non-Spherical Nuclei

Factor	**Disk q = 0.5**	**Ellipsoid q = 0.5**	**Disk q = 0.333**	**Ellipsoid q = 0.333**
$K_{\Delta G^*}$	0.75	0.688	0.5	0.481
K_{β^*}	1	0.875	0.833	0.778
K_Z	1.155	1.206	1.414	1.441
$K_{\beta^*} \times K_Z$	1.155	1.055	1.179	1.121

the factor $K_{\Delta G^*}$ is most important with regard to the nucleation rate because it appears in an exponential term.

The nucleation rate J (Equation (1)) is related to the steady-state nucleation rate J_0 through an incubation factor $\exp(-\tau/t)$, which quantifies the transient during which metastable embryos with sub-critical radii are formed. The time constant τ in this term is given by the following equation [34, 37]:

$$\tau = \frac{\pi R T r^{*3}}{96 V_M D \sigma} \quad . \tag{6}$$

R and V_M denote the gas constant and the molar volume of the precipitate, respectively.

In a strict sense, the above equations pertain to *two-component* alloys. Methods used to establish effective values for parameters such as C, D, σ, ΔG^* for use in simulations for 718 are discussed in Section III.

B. *Diffusional Growth*

Following nucleation, the diffusional growth of spherical γ' and disk/ellipsoidal γ'' precipitates was described using solutions to the one-dimensional diffusion equation. Both approaches were base on the so-called exact solution developed by Carslaw and Jaeger [38] and Aaron, *et al.* [39] for the growth of an isolated spherical particle.

1. Growth of γ'

Following nucleation, the rate of diffusional growth of a (spherical) γ' precipitate in a matrix with a finite supersaturation was described by [38, 39]:

$$dr_{\gamma'}/dt = 2\lambda^2 D / r_{\gamma'} \quad . \tag{7}$$

200 in which $r_{\gamma'}(t)$ denotes the γ' particle radius as a function of time t, D is the
201 diffusivity, and λ^2 is the growth-rate parameter, which takes the place of the
202 supersaturation Ω found in various solutions to the diffusion equation:

203 $$\Omega = (C_M - C_I)/(C_P - C_I) \text{ .} \quad (8)$$

204 C_M, C_I, and C_P comprise the matrix composition far from the matrix-precipitate
205 interface, the matrix at this interface, and the precipitate at the interface,
206 respectively. For diffusion-controlled growth, C_I and C_P denote the equilibrium
207 matrix and precipitate compositions, respectively. The parameters λ and Ω are
208 interrelated by

209 $$\{\lambda^2 \exp(\lambda^2)\} \bullet [\, (\exp(-\lambda^2)) - (\lambda\pi^{1/2}\mathrm{erfc}(\lambda))] = \Omega/2 \text{ ,} \quad (9)$$

210 a relation which cannot be inverted to obtain an analytical expression for λ^2 as a
211 function of Ω. Therefore, the value of Ω for a number of closely-spaced values of
212 λ were calculated in the present work, and a sixth-order polynomial was fit to
213 describe the functional dependence of λ^2 on Ω.

214 For an ensemble of γ' precipitates, the effect of soft impingement on the
215 'far-field' matrix composition C_M was taken into account using the usual
216 approximation (derived from mass balance considerations [40]) which implicitly
217 assumes a uniform solute concentration in both the particle and the matrix, viz.,

218 $$C_M = (C_o - f_{\gamma'}C_{\gamma'} - f_{\gamma''}C_{\gamma''})/(1 - f_{\gamma'} - f_{\gamma''}) \text{ ,} \quad (10)$$

219 Here, C_o, $C_{\gamma'}$, and $C_{\gamma''}$ are the compositions of the overall alloy, γ', and γ'',
220 respectively, and $f_{\gamma'}$ and $f_{\gamma''}$ represent the volume fractions of the respective
221 phases. As will be described in Section III, the composition of each of the

precipitate phases was assumed to be constant and thus equal to C_P in the respective equations for the supersaturation (Equation (8)) for a given alloying element.

2. Growth of γ''

The diffusional growth of γ'' was modeled in a manner similar to that described for γ' in the previous section. The principal difference related to the morphology of the γ'' precipitates. For simplicity, γ'' particles were assumed to be oblate ellipsoids having an assumed-constant aspect ratio A = Y/X ~1/q, in which Y and X denote the semi-lengths of the major and minor axes, respectively.

The diffusion solution for the growth of an oblate ellipsoid of constant aspect ratio A is the following [41-44]:

$$Y = 2A(\beta Dt)^{1/2} \quad \text{and} \quad X = 2(\beta Dt)^{1/2} \tag{11}$$

or,

$$dY/dt = (2A^2\beta D/Y) \quad \text{and} \quad dX/dt = 2\,\beta D/X \tag{12}$$

As for the growth of spherical particles, the diffusion solution for an ellipsoidal particle involves a growth-rate parameter denoted as β in Equations (11) and (12). β is related to the supersaturation Ω as follows:

$$\Omega = [\exp(\beta)][\beta^{3/2} A^2] \int_{u=\beta}^{u=\infty} \frac{[\exp(-u)]du}{\{\beta(A^2-1)+u\}u^{1/2}} \quad . \tag{13}$$

Similar to the challenge associated with determining $\lambda^2(\Omega)$ for spherical precipitates, Equation (13) is not readily inverted to obtain $\beta(\Omega)$. Because the expression involves an integral, a Microsoft Visual Basic program was written to determine the desired functional dependence [45].

To simplify numerical calculations, an artifice (introduced in Reference 45) was utilized to enable the growth of ellipsoidal γ'' precipitates to be described in terms of spherical particles with an effective radius $r_{\gamma''eff}$. The procedure for defining $r_{\gamma''eff}$ was based on determining the time rate of change of the volume of the ellipsoidal particle ($V_e = (4/3)\pi Y^2 X$). Using Equations (11) and (12), this rate is readily determined to be the following:

$$\frac{dV_e}{dt} = 8\pi A^2 \beta D X \quad . \tag{14}$$

The corresponding equation for the volumetric rate of growth of a sphere was derived form Equation (7) and the relation for the volume of a sphere of radius r_{eff} [$V_s = (4/3)\pi(r_{eff})^3$], thus yielding dV_s/dt :

$$\frac{dV_s}{dt} = 8\pi\lambda^2 D r_{eff} \tag{15}$$

Combining Equations (14) and (15), $r_{\gamma''eff}$ is thus

$$r_{\gamma''eff} = (A^2\beta/\lambda^2)X \tag{16}$$

$$= (A\beta/\lambda^2)Y$$

The factor $A\beta/\lambda^2$ was found to be nearly constant for the range of supersaturations and typical precipitate geometries (i.e., $2<A<3$, or $0.33<(1/A)<0.5$) encountered for the diffusional growth of γ''. In particular, for A = 2, $\beta/\lambda^2 = 0.435$, and $r_{\gamma''eff} = 0.87Y$. For A = 3, $\beta/\lambda^2 = 0.298$, and $r_{\gamma''eff} = 0.885Y$. Thus, to a good approximation, the growth of ellipsoidal particles can be simulated in a fashion identical to that used for spherical particles by assuming

they have an effective radius equal to 0.88 times the length of the semi-major axis (Y).

C. *Coarsening*

Coarsening kinetics are relatively slow and the driving force is relatively less compared to those for N&G at typical aging temperatures. Therefore, it was assumed that coarsening of 718 occurred after ~98 pct of the precipitate volume fraction had been formed and was thus treated to a first order as a distinct (final) stage in the heat-treatment process. The rate of increase of the average precipitate size was quantified using the modified LSW theory.

For *spherical* precipitates such as γ', the kinetics are expressed as follows [46-48]:

$$\bar{r}^3 - \bar{r}_o^3 = K_{MLSW}\, t \qquad (17)$$

$$K_{MLSW} = \frac{8w(f_{\gamma'})D\sigma C_\gamma (1-C_\gamma)V_M}{9RT(C_{\gamma'}-C_\gamma)^2[1+\partial \ln v/\partial \ln C_\gamma]} \qquad (18a)$$

The terms $\bar{r}$ and $\bar{r}_o$ represent the *average* instantaneous precipitate radius and radius at the end of N&G, respectively. In the equation for the modified rate constant, K_{MLSW}, $w(f_{\gamma'})$ denotes the factor needed to correct for the finite volume fraction of γ' particles, C_γ and $C_{\gamma'}$, are the equilibrium concentrations of the rate-limiting solute in the matrix and γ' precipitate, respectively, and the bracketed term is the thermodynamic factor in which v is the activity coefficient for the rate-limiting solute in the γ matrix. In the present work, the volume-fraction function w was chosen to follow the form proposed by Voorhees and Glicksman [49], e.g., w(0.04) ~ 1.23 and w(0.11) ~ 1.6.

An identical rate equation pertains to the coarsening of γ''. Taking the precipitates to be disk shape with an average radius $\bar{r}$ and aspect ratio of q (=$2h_{\gamma''}/2r_{\gamma''}$), the pertinent expression for the rate constant K_{MLSW} in Equation (17) was deduced from the relation of Boyd and Nicholson [50] modified to include terms (as in Equation (18a) to correct for the finite volume fraction of precipitates and the fact that the phases are not terminal solid solutions [48, 49]:

$$K_{MLSW} = \frac{16w(f_{\gamma''})D\sigma C_{\gamma}(1-C_{\gamma})V_M}{9\pi qRT(C_{\gamma''}-C_{\gamma})^2[1+\partial \ln v/\partial \ln C_{\gamma}]} \qquad (18b)$$

In Equation (18b), $C_{\gamma''}$ is the equilibrium concentration of the rate-limiting solute in the precipitate, and the other terms are as defined previously. In particular, σ is the energy along the lateral surface of the γ''-γ interface. Equation (17) is also sometimes written in terms of the change in disk diameter L = $2r_{\gamma''}$, in which case the numerical pre-factor in Equation (18b) is $128/9\pi$ instead of $16/9\pi$.

Because Equations (18) were applied to verify reasonable values of an effective diffusivity, it was necessary to quantify the effect of all solutes on the coarsening rate constant. In this regard, it has been shown that rapidly diffusing solutes can also influence the coarsening rate [51]. Based on this prior work, it can be concluded that the effective rate constant K_{eff} is equal to the inverse of the sum of the inverse rate constants for each of the individual solutes, i.e.,

$$\frac{1}{K_{eff}} = \frac{1}{K_1} + \frac{1}{K_2} + \frac{1}{K_3} + \ldots \qquad (19)$$

III. INPUT DATA FOR SIMULATIONS

As can be inferred from the discussion in Section II, the simulation of precipitation for superalloy 718 requires a large number of material parameters. These include the phase equilibria/phase fractions and phase compositions, ΔG^* and ΔG_{el}, interface energies, effective diffusivities, etc. for both γ'' and γ'. The selections of values for these quantities are described in the following sections.

A. Phase Equilibria and Phase Compositions

Fast-acting simulations of precipitation, such as that developed in the present work, often rely on measured or calculated phase-equilibria data in the form of phase fractions as a function of temperature and (assumed constant) precipitate compositions. Unfortunately, there are wide variations in these quantities in the literature, some of which have been ascribed to relatively-small changes in exact alloy composition, changes in the ratio of Al+Ti to Nb contents (in atomic percent) [13, 14] , and the specific characterization method that was used. Hence, the literature measurements were analyzed to arrive at what can be considered *typical* values. Furthermore, as in previous mean-field simulations of γ''/γ' precipitation in 718 [29-31], it was assumed that the phases were discrete entities despite the fact that γ'' particles often include some γ', thus forming a composite structure [13, 14].

Equilibrium phase fractions as a function of temperature (Figure 1) were deduced from measurements summarized in References 13, 14, and 52-58. In deriving this plot, more emphasis was given to direct measurements of the lenticular phase (taken to be γ'') and spheroidal phase (assumed to be γ')

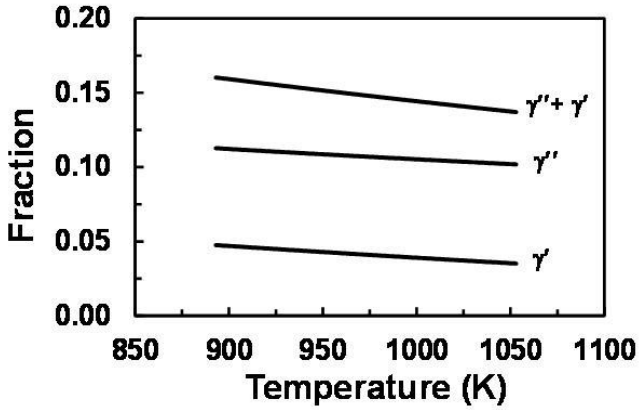

Figure 1. Equilibrium fractions of the γ'' and γ' phases as a function of temperature.

observed via transmission electron microscopy or high-resolution scanning electron microscopy. As pointed out by Lawitsky, *et al.* [58], atom-probe tomography (APT) tends to exaggerate volume fraction magnitudes unless careful consideration is given to variations in evaporation rates, mass balance considerations, etc.

Typical compositions of the overall alloy and the γ'' and γ' phases are summarized in Table II. The precipitate chemistries were based on atom-probe measurements [58, 59], modified slightly to ensure mass-balance consistency with the overall alloy composition. Using these compositions and an assumed (approximate) density of ~8300 kg/m^3 for each phase, the molar volumes (V_M)

Table II. Compositions Used in the Present Work

Material	Fe	Cr	Mo	Nb	Ti	Al	Ni
Overall (w/o)	20.7	18	3	5.3	0.97	0.57	Bal
Overall (a/o)	21.5	20	1.76	3.31	1.18	1.24	Bal
γ'' (a/o)	1.9	2.18	2.0	18.5	4.3	1.2	Bal
γ' (a/o)	2.3	1.95	1.1	7.38	7.86	8.95	Bal

were estimated to be 7.84 x 10^{-6} m^3 and 6.93 x 10^{-6} m^3 for γ'' and γ' precipitates, respectively.

B. *Free Energy of Transformation (ΔG^*) and Elastic Strain Energy (ΔG_{el})*

The free energy of transformation per mole of precipitate (ΔG^*) was estimated using classical expressions from solution thermodynamics [15]. For the case in which the precipitate is *enriched* in solute relative to the matrix phase, ΔG^* for γ'' precipitates is given by:

$$\Delta G^*(\gamma \rightarrow \gamma'') = -\frac{(C_{\gamma''} - C_\gamma)RT\ln(C_\gamma/C_M)}{(1-C_\gamma)[1+\partial \ln v/\partial \ln C_\gamma]} \qquad (20a)$$

A similar relation applies when the precipitate is depleted in solute, i.e.,

$$\Delta G^*(\gamma \rightarrow \gamma'') = -\frac{(C_\gamma - C_{\gamma''})RT\ln[(1-C_\gamma)/(1-C_M)]}{C_\gamma[1+\partial \ln v/\partial \ln C_\gamma]}. \qquad (20b)$$

In Equations (20a) and (20b), all of the terms are the same as defined above. Identical expressions pertain to γ' precipitates with the exception that $C_{\gamma''}$ is replaced by $C_{\gamma'}$ in all places in the two equations.

Values of the thermodynamic factor (TF) (based on CALPHAD/thermodynamic calculations) and ΔG^* for each solute in 718 for the case in which the instantaneous γ-matrix composition (C_M) is equal to the overall alloy composition (corresponding to the onset of precipitation) are summarized in Table III. Not surprising, alloying elements which are the most highly partitioned between the matrix and the corresponding precipitate phase give rise to the largest values of ΔG^* and thus provide the greatest driving force for nucleation. Specifically, an inspection of the results in Table III shows that Nb and Ti are

Table III. Values of the Thermodynamic Factors (TF) and ΔG^*

Element	TF	γ'' ΔG^* (J/mol)	γ' ΔG^* (J/mol)
Fe	0.82	399	392
Cr	0.91	317	3
Mo	0.92	~0	~0
Nb	1.94	756	271
Ti	1.30	219	423
Al	1.25	8	176

most likely the solutes that control nucleation for γ'' and γ', respectively. Additional thermodynamic calculations indicated relatively-limited changes in TF with changes in matrix composition as precipitation progressed, and thus were neglected in the calculation of ΔG^* during N&G simulations.

The magnitude of ΔG_{el} during the nucleation of γ'' precipitates is difficult to quantify because of large changes in the aspect ratio q at small particle sizes [60] and possible changes in phase composition with growth, factors which are not treated explicitly in the present approach. Nevertheless, several estimates were obtained using Equation (3) for two cases, taking μ = 62 GPa and υ = 0.3 in both. For the first, it was assumed that the nucleus was essentially equiaxed (q = 1) and a uniform dilation of 0.0258 (=3x0.0086) pertained [61], thus yielding ΔG_{el} = 17 MPa. In the other case, it was assumed that the strain field comprised solely a tetragonal distortion along the c axis of a magnitude suggested by the *small-particle* data of Sundararaman, *et al.* [14] (i.e., ~0.01), thereby leading to ΔG_{el} = 7 MPa. Baseline simulations were thus performed using an average of these two values, 12 MPa (~94 J/mol). With this specification, the magnitude of the elastic

375 strain energy was ~12 percent of the chemical free energy ΔG^* (per the Nb value
376 in Table III) during the early stages of γ'' precipitation. The effect of uncertainty in
377 the elastic strain energy on simulation predictions is examined further in the
378 sensitivity analysis in Section IV below.

379 Because the misfit between γ' and the γ matrix is relatively small, ΔG_{el}
380 was neglected in the γ' nucleation analysis or assumed to be accounted for via
381 small adjustments of the γ'-γ interface energy, a procedure which is typical for
382 low-misfit γ' precipitates in PM γ-γ' nickel-base superalloys.

383 C. *Effective Diffusivities*

384 Effective diffusivities for the present precipitation analysis were
385 established based on 718/Rene88DT diffusion-couple data [62], which were tuned
386 to replicate measured values of the coarsening-rate constant for coherent γ'' and
387 γ' precipitates [52, 60]. Diffusivities fitted using measured concentration profiles
388 developed in 718 at 1423 K are summarized in Table IV [62]. The corresponding
389 values at the much lower temperatures used for aging of 718 were estimated

Table IV. Experimentally-Fitted Effective Diffusivity of Solutes in Alloy 718 at 1423 K (1150 °C) [62]

Element	Diffusivity (m^2/s)
Fe	1.56×10^{-14}
Cr	1.58×10^{-14}
Mo	1.66×10^{-14}
Nb	6.69×10^{-14}
Ti	2.02×10^{-14}
Al	1.36×10^{-14}

using an activation energy (Q_d) for each solute of 285 kJ/mol [63] to obtain expressions for the diffusivity of solute X of the form:

$$D_X = D_{czh}\exp[(Q_d/R)(\frac{1}{T}-\frac{1}{1423})] \quad (21)$$

Here, the coefficient D_{czh} denotes the pertinent diffusivity at 1423 K in Table IV.

1. *Tuning of diffusivity using coarsening data*

An initial attempt to predict observed coarsening rates for γ'' (in terms of L = $2r_{\gamma''}$) at temperatures of 943 K, 973 K, and 1003 K [60] per Equations (18b) and (19) was made using (i) the measured diffusivities (extrapolated to the pertinent temperatures per Equation (21)), (ii) a value of interface energy of 56 mJ/m^2 (deduced from initial N&G calculations), and (iii) q ~ 0.32-0.45, the specific value chosen to be appropriate to the measured size ranges of the coherent precipitates. This first try yielded predictions that were *high* by a factor of ~1.6. After reducing each diffusivity by this amount, approximate agreement with the measured rate constants was obtained (Table V). Specifically, for temperatures of 943 K and 1003 K, the predicted rate constant based on all solutes was somewhat below the measurement; at 973 K the prediction exceeded the measurement. With diffusivities fitted thusly, however, the N&G calculations gave extremely-poor predictions of measured precipitate sizes and transformation kinetics.

A considerably better fit of the γ'' coarsening data was obtained by realizing that the prior diffusivity measurements (Table IV) corresponded to a situation in which all of the solutes were diffusing in the same direction. Thus, the

Table V. Predicted Values of the Coarsening Rate Constant K_d (in nm^3/s) for γ'' as a Function of Temperature*

Element	943 K	973 K	1003 K
Fe	0.176	0.588	2.04
Cr	0.183	0.612	2.13
Mo	14.6	48.9	169.3
Nb	0.0421	0.141	0.498
Ti	0.0739	0.247	0.866
Al	31.6	105.7	370.7
All Solutes	**0.0206**	**0.0689**	**0.242**
Measurement [60]	**0.0174**	**0.083**	**0.229**

* All diffusivities multiplied by a factor of 0.625; σ = 56 mJ/m^2, q = 0.45 (943 K), 0.40 (973 K), or 0.32 (1003 K)

412 effect of off-diagonal terms in the diffusivity matrix on behavior was not captured.
413 In particular, the nucleation, growth, and coarsening of γ'' (and γ') both involve
414 diffusion of Cr in a direction *opposite* to that of solutes partitioning to the
415 precipitate phase(s). Specifically, a tendency for Cr to partially diffuse down
416 gradients in Nb, Ti, etc., would result on in an effective diffusivity of Cr that could
417 be considerably *lower*. Such a reduction in effective diffusivity, for example, has
418 been found in the analysis of precipitation and coarsening for various commercial
419 superalloys and NiAlCr-X single crystals [21, 64]. Based on the initial N&G
420 calculations, a reduction of the diffusivity of Cr by a factor of 10, without any
421 adjustment for the other diffusivities, provided excellent agreement between the
422 measured rate constant for the coarsening of γ'' at 943 K and that predicted
423 based on all solutes (bold entries in Table VI). For the other two temperatures
424 (973 K and 1003 K), the measured rate constant was slightly greater than the

Table VI. Predicted Values of the Coarsening Rate Constant K_d (in nm^3/s) for γ'' as a Function of Temperature*

Element	943 K	973 K	1003 K
Fe	0.281	0.940	3.27
Cr	**0.0293**	**0.0981**	**0.341**
Mo	23.4	78.3	270.9
Nb	0.0805	0.269	0.951
Ti	0.211	0.707	2.48
Al	50.6	169.2	593.1
All Solutes	**0.0182**	**0.0609**	**0.213**
Measurement [60]	**0.0174**	**0.083**	**0.229**

* Chromium diffusivity multiplied by a factor of 0.1; σ = 56 mJ/m^2, q = 0.45 (943 K), 0.40 (973 K), or 0.32 (1003 K)

Table VII. Predicted Values of the Coarsening Rate Constant K_r (in nm^3/s) for γ' as a Function of Temperature*

Element	973 K	1023 K
Fe	0.0362	0.193
Cr	**0.00378**	**0.0201**
Mo	2.98	15.8
Nb	0.0572	0.313
Ti	0.00388	0.0209
Al	0.0102	0.0552
All Solutes	**0.00150**	**0.00805**
Measurement [52]	**0.00261**	**0.0129**

* Chromium diffusivity multiplied by a factor of 0.1, σ = 40 mJ/m^2.

prediction based on all solutes but less than that based on the single (rate-limiting) solute (Cr) (bold entries in Table VI).

Using the same adjustment for the diffusivity of Cr, predictions of the coarsening rate constants for γ' at 973 K and 1023 K showed good agreement with the measurements of Han [52] when represented in r^3 vs t terms (Table VII).

At both temperatures, the measured value lay between the prediction based on all solutes and that based on the rate-limiting solute (Cr), in all cases assuming an interface energy of 40 mJ/m^2.

2. *Off-diagonal diffusivity influence*

The efficacy of the above adjustment to the effective diffusivity of chromium for the interpretation of coarsening observations was rationalized within the context of the phenomenological (Fick's-Law) description of diffusion, which incorporates both diagonal and off-diagonal diffusivity terms. For Cr, this relation is as follows:

$$\tilde{J}_{Cr} = -\tilde{D}^{Ni}_{Cr,Cr}\frac{\partial C_{Cr}}{\partial X} - \tilde{D}^{Ni}_{Cr,Nb}\frac{\partial C_{Nb}}{\partial X} - \tilde{D}^{Ni}_{Cr,Al}\frac{\partial C_{Al}}{\partial X} + \ldots \quad (22)$$

Here, $\tilde{J}_{Cr}$ is the chromium flux, and each of the terms $-\tilde{D}^{Ni}_{Cr,i}\frac{\partial C_i}{\partial X}$ (i = Cr, Nb, Al, Fe, …) denotes the contribution to this flux associated with the diffusivity and concentration gradient of a given solute i. Thus, *positive* values of the off-diagonal diffusivities and concentration gradients of a sign *opposite* to that of Cr can reduce the overall Cr flux.

Diffusion couple data for Ni-Cr-Nb, Ni-Cr-Al, and Ni-Fe-Co-Cr alloys [65-68] provided insight into off-diagonal effects pertinent to the present work. For example, Xu, *et al.* [66] found that $\tilde{D}^{Ni}_{Cr,Nb}$ at 1273 K was of the order of 4 x 10^{-15} m^2/s for an alloy with comparable matrix composition to that developed in 718 (i.e., 20 a/o Cr and 1.5 a/o Nb). This value is *greater* than $\tilde{D}^{Ni}_{Cr,Cr}$ obtained from an extrapolation to 1273 K of the measurement of Campbell, *et al.* [62] per Equation (21), i.e., 0.92 x 10^{-15} m^2/s. It may thus be surmised that the large Cr

concentration and hence its larger concentration gradient relative to that of Nb likely mitigates the tendency for Cr to diffuse down the Nb concentration gradient. By contrast, Xu *et al*. [66] found that $\tilde{D}^{Ni}_{Nb,Cr}$ was an order of magnitude *less* than $\tilde{D}^{Ni}_{Cr,Nb}$. This result, coupled with the high value of $\tilde{D}^{Ni}_{Nb,Nb}$ (Table IV) (and perhaps the influence of other elements diffusing in the same direction), may lead one to hypothesize a minimum effect of off-diagonal terms on the effective diffusivity of niobium.

The off-diagonal effect of aluminum on the diffusion of Cr was quantified by Nesbitt and Heckel [67]. In this effort, various measurements revealed $\tilde{D}^{Ni}_{Cr,Al}$ / $\tilde{D}^{Ni}_{Cr,Cr}$ was of the order of 0.8 to 1.8, but $\tilde{D}^{Ni}_{Al,Cr}$ / $\tilde{D}^{Ni}_{Al,Al}$ was only 0.3. Similar to Nb, the 718/Rene 88DT diffusion-couple data reported by Campbell, *et al.* [62], involved diffusion of Cr in a direction opposite to that of Al, in contrast to its behavior during the precipitation of γ''. However, due to the formation of composite γ''/γ' precipitates, the off-diagonal diffusivity of Al likely has limited effect on the effective diffusivity of Cr, at least for the description of γ'' precipitation.

With regard to the formation of γ', the low value of $\tilde{D}^{Ni}_{Al,Cr}$ / $\tilde{D}^{Ni}_{Al,Al}$ reported by Nesbitt and Heckel [67]. suggests a limited off-diagonal effect of Cr on Al diffusion, which is likely already included in the experimental measurement of Campbell, *et al.* [62]. Last, the off-diagonal diffusivity $\tilde{D}^{Ni}_{Cr,Fe}$ has been determined to be very small [68]. Because Fe diffused in the same direction as Cr in the 718/Rene 88DT diffusion-couple data, as it does during precipitation heat

474 treatment, the diffusivity of Campbell, *et al.* [62] also likely already includes the
475 effect of the Fe off-diagonal term on the effective diffusivity of Cr.

476 D. *Interface Energies*

477 As will be discussed further in Section IV, the interface energy σ affects
478 the nucleation rate to the third power in an exponential term. Therefore, its
479 precise value has a very significant impact on precipitation kinetics. N&G
480 simulations with interface energies of 56 mJ/m^2 for γ''-γ and 40 mJ/m^2 for γ'-γ
481 provided very good agreement with the volume-fraction-versus-time
482 measurements of Han [52]. The former value for the lateral γ''-γ interfaces is
483 comparable to that suggested by Zhang, *et al.* [30] for 718 (55 mJ/m^2) and by
484 Moore, et al. [27] for alloy 625 (up to 51.8 mJ/m^2). The value for γ'-γ interfaces is
485 higher than that typically found in the literature for PM γ-γ' superalloys (i.e., ~23
486 to 32 mJ/m^2) [18, 21, 69], but may be a result of the high niobium content in γ' in 718
487 (~7.5 a/o) compared to that in the PM alloys (i.e., ~1 to 2 a/o) [70] or the lower
488 temperature at which precipitation occurs in 718 compared to that for γ-γ'
489 superalloys

490 **IV. VALIDATION AND SENSITIVITY ANALYSIS**

491 A *Simulation Approach*

492 Simulations of the simultaneous nucleation and growth of γ'' and γ' during
493 aging of superalloy 718 were performed using a numerical, fast-acting
494 (spreadsheet) approach. The method, based on the original work of Kampmann
495 and Wagner [71], was developed and applied previously for describing the
496 precipitation of γ' during continuous cooling of the PM superalloy LSHR [21]. In

497 brief, the method comprised steps of nucleation and growth that were used to
498 populate a series of bins, each with a given size of precipitate. For γ'', the solute
499 controlling nucleation was niobium (Table III); chromium (with its minimum values
500 of $D\Omega$) was taken to control growth. For γ', titanium controlled nucleation (Table
501 III) and aluminum was rate limiting for growth. For both precipitate classes, Ni
502 was assumed to be the solvent (with an atomic fraction of ~0.5) and the value of
503 C in the nucleation relation (Equation (1)) was taken to be 0.5.

504 The time increment for the simulations was chosen to minimize the total
505 number of bins required. The principal change to the procedure in the present
506 work related to the coupling of the matrix composition (mass-balance)
507 calculations (Equation (10)) for the two different phases with one important
508 exception. Specifically, the precipitation of γ'' involves the rejection of aluminum
509 which may then contribute to the formation of composite (γ''-γ') particles [13, 14].
510 Therefore, the γ''-precipitation contribution to the aluminum matrix composition in
511 Equation (10) (needed to simulate the growth of γ') was neglected. It was also
512 determined that the incubation time for nucleation of both γ'' and γ' (Equation (6))
513 was very short (typically of the order of 1 s) compared to the time steps used in
514 the simulations and was therefore neglected.

515 B. *Comparison with Experiments*

516 The present simulations using the *baseline* material coefficients
517 summarized in Section III focused on precipitation predictions which were
518 compared to the observations of Han [52] for a lot of 718 that was super-δ-solvus
519 solution treated, water quenched, and aged at 973 K. Key predictions comprised

the temporal variation of the total volume fraction (normalized by the assumed equilibrium total volume fraction), the average size of the γ'' and γ' precipitates, and the volume fraction ratio ($f_{\gamma''}/f_{\gamma'}$). A number of additional simulations of aging kinetics were also performed and compared to *in-situ* experimental measurements (based on dynamic Young's modulus and neutron-diffraction techniques), but are discussed in detail in a companion paper [72].

Volume-fraction predictions at 973 K for the baseline input data (smooth black line in Figure 2a) showed a relatively-good fit with the measurements. In addition, the predicted average precipitate diameters (converted to disk diameter from simulations based on the effective radius for γ'' and the directly-simulated values of 2r for γ') for a time of 25 h (at which the total volume fraction reached 98 percent of the assumed equilibrium fraction) were 28.1 nm for γ'' and 14.3 nm for γ' (black curves in Figure 2b). To enable a comparison with the shortest-time

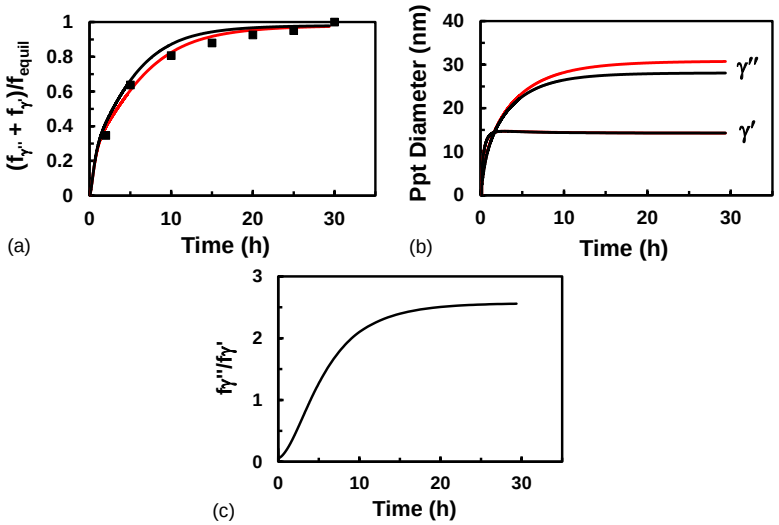

Figure 2. Fast-acting-simulation predictions of the temporal evolution of (a) the normalized total volume fraction, (b) precipitate diameters, and (c) ratio of the volume fractions of γ'' and γ' during aging at 973 K. Simulation predictions correspond to the baseline (black curves) or modified-baseline (red curves) input datasets. The predictions in (a) are compared to measurements by Han [52] (data points).

(50-h) measurement reported by Han [52], the predicted diameters were assumed to increase via static coarsening for an additional 25 h per Equation (17) and the measured rate constants (Tables VI and VII). The sizes so obtained (30.8 nm for γ'' and 14.7 nm for γ') showed reasonable overall agreement with the measurements of 25.7 and 14.3 nm, respectively. Last, simulations suggested that the volume-fraction ratio was initially less than unity, but increased to the nominal equilibrium ratio at longer times (Figure 2c).

C. *Sensitivity Analysis*

The sensitivity of the kinetic predictions at 973 K (Section IV.B) with respect to several key input parameters was assessed via a number of fast-acting simulations. These parameters comprised the values of the interface energies and diffusivities for both γ'' and γ', the ΔG_{el} for the formation of γ'', and the thermodynamic factor of Nb in nickel solid solution.

1. *Interface energies*

The influence of a relatively-small change in interface energy of ± 1.5 mJ/m^2 relative to that in the baseline input dataset (whose magnitude would not noticeably affect the interpretation of the coarsening results in Tables V, VI, and VII) on overall aging kinetics (in terms of $(f_{\gamma''}+f_{\gamma'})/f_{equil}$), the diameter of the precipitates, and the volume-fraction ratio is illustrated in Figures 3 and 4. For a variation in $\sigma_{\gamma''\text{-}\gamma}$ relative to the baseline of 56 mJ/m^2, the aging kinetics (Figure 3a) showed a considerable increase or decrease in rate for the lower or higher values of $\sigma_{\gamma''\text{-}\gamma}$, respectively. This dependence can be ascribed to the markedly enhanced or retarded rates of nucleation, respectively, which in turn led to

noticeably smaller or larger average diameters of the γ'' precipitates with little effect on the size of the γ' precipitates (Figure 3b). (The negligible effect on γ' diameter was likely related to the modification of the mean field-field matrix-composition for the growth-rate limiting solute for γ' (i.e., Al) as discussed in Section IV.A.) Not surprisingly, the enhancement of γ'' nucleation with lower interface energy was also associated with an initially-higher $f_{\gamma''}/f_{\gamma'}$ ratio and a more rapid approach to the equilibrium value of this quantity (Figure 3c).

When $\sigma_{\gamma'\text{-}\gamma}$ was decreased or increased by $\pm$1.5 mJ/m^2 (Figure 4), the aging kinetics at short times (~0 to 1.5 h) were increased or decreased, respectively (Figure 4a). At longer times (> 1.5 h), the growth of γ'' likely started to dominate behavior, and the apparent effect of $\sigma_{\gamma'\text{-}\gamma}$ was masked, thereby

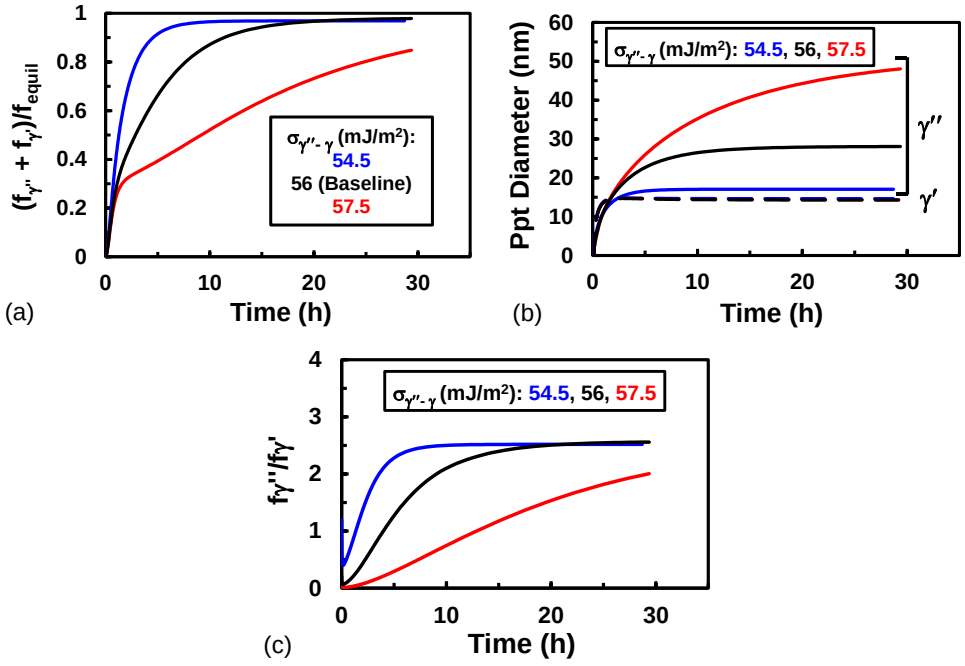

Figure 3. Fast-acting-simulation predictions of the effect of a $\pm$1.5 mJ/m^2 variation in $\sigma_{\gamma''\text{-}\gamma}$ on the temporal evolution of (a) the normalized total volume fraction, (b) precipitate diameters, and (c) ratio of the volume fractions of γ'' and γ' during aging at 973 K.

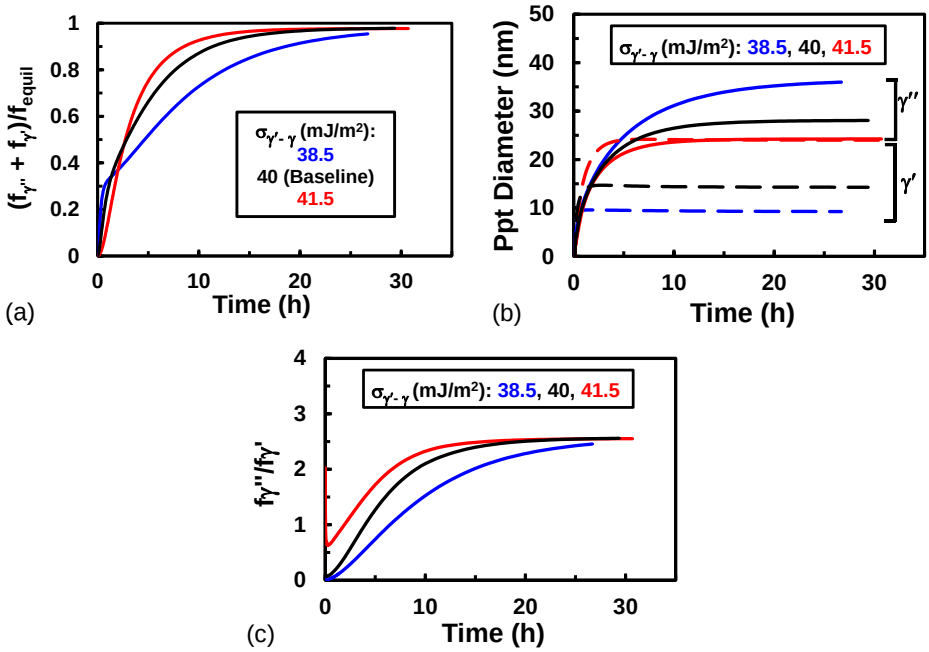

Figure 4. Fast-acting-simulation predictions of the effect of a ±1.5 mJ/m^2 variation in $\sigma_{\gamma'-\gamma}$ on the temporal evolution of (a) the normalized total volume fraction, (b) precipitate diameters, and (c) ratio of the volume fractions of γ'' and γ' during aging at 973 K.

giving rise to a crossover in kinetics. Furthermore, simulations revealed that the average diameter of γ' was predicted to increase or decrease with an increase or decrease in $\sigma_{\gamma'-\gamma}$, as expected due to the influence of interface energy on nucleation. The accompanying growth dependence of γ'' on $\sigma_{\gamma'-\gamma}$ was the opposite, likely because of the indirect effect of γ' growth on matrix composition (calculated per Equation (10)) and resulting changes in the evolution of the supersaturation which controls γ''.

The very large effect of small variations in $\sigma_{\gamma''-\gamma}$ or $\sigma_{\gamma'-\gamma}$ on precipitation kinetics and nucleation in particular is related to its appearance in an exponential term in Equation (1). Replacing r* by its definition in Equation (2), the argument of the pertinent exponential becomes the following:

$$-\frac{16\pi\sigma^3 K_{\Delta G^*}}{3k_B T(\Delta G^* + \Delta G_{el})^2} \quad (23)$$

This expression shows that the large influence of σ on nucleation rate is enhanced by its cubic dependence. Despite the fact that some of the uncertainty in σ has been avoided in the present work by ensuring that (long-time) coarsening observations are independently corroborated, Equation (23) indicates that small errors in the selection of σ can be mitigated (or further confounded) by corresponding errors in either $K_{\Delta G^*}$ or, more likely, the free energies in the denominator because of their square dependence. Uncertainties in ΔG^* (Equations (20a) and (20b)) can be mitigated somewhat by direct measurement of the enthalpy of transformation (ΔH^*) and the determination of the corresponding entropy (ΔS^*) from knowledge of the solvus temperatures, as was demonstrated in Reference 21. The overlapping of the transformation range of γ'' and γ', however, tends to complicate the use of this alternate method for estimating ΔG^* of each of the two strengthening precipitates in 718. Despite this challenge, research to refine and validate thermodynamic calculations for 718 is ongoing and will be addressed in a future communication.

2. *ΔG_{el} and the thermodynamic factor of Nb*

Possible errors/uncertainties in ΔG_{el} for the precipitation of γ'' were assessed via a separate suite of calculations. In particular, three levels of ΔG_{el} were used (17, 25.5, and 70 MPa) which corresponded to elastic deformations comprising the dilation suggested in Ref. 61 plus a tetragonal distortion along the

599 c axis of 0, 0.005, or 0.0227, respectively. The second of the two levels of
600 tetragonality pertains to that obtained by extrapolating the data in Ref. 14 to the
601 size of the critical nucleus, and the third is that reported in Ref. 61. Maintaining all
602 of the other simulation parameters the same as before, predictions of the
603 normalized volume fraction as a function of time for heat treatment at 973 K
604 deviated sharply from the measurements and led to predicted γ'' diameters two
605 or more times as great as the baseline case (for which ΔG_{el} = 12 MPa). This
606 trend resulted from a *reduction* in γ'' nucleation rate due to the reduced net
607 driving force ($\Delta G^* + \Delta G_{el}$).

608 Three additional cases for which $\sigma_{\gamma''-\gamma}$ was reduced in concert with the
609 above levels of ΔG_{el} (to reproduce observed transformation kinetics at least
610 approximately) were also investigated. The required interface energies and
611 precipitate sizes are summarized in Table VIII. These results indicated that
612 similar responses in terms of predicted average γ'' size were obtained only for
613 the cases involving modest decreases in the required level of $\sigma_{\gamma''-\gamma}$ (of the order
614 of 10 pct.) corresponding to ΔG_{el} = 17 and 25.5 MPa. Such decreases would

Table VIII. Sensitivity Analysis for ΔG_{el}

ΔG_{el} (MPa)	$\sigma_{\gamma''-\gamma}$ (mJ/m^2)	γ'' Diameter (nm)	γ'' Diameter (nm)
12	56.0	28.1	14.3
17	53.8	31.9	14.3
25.5	49.8	32.6	14.3
70	25.3	44.6	14.3

615 require correspondingly small increases in effective diffusivity to maintain
616 comparable agreement between the predicted and measured rate constants for
617 the coarsening of γ'' (Table VI).

618 In contrast to the cases of ΔG_{el} = 17 and 25.5 MPa, the much more
619 substantial increase in ΔG_{el} to 70 MPa would require that the γ''-γ interface
620 energy be approximately halved in order to reproduce the observed precipitation
621 kinetics. However, such a change was predicted to result in an average γ''
622 diameter substantially higher than the measured value, as shown in Table VIII. It
623 would also entail a much higher value of effective diffusivity in order to maintain
624 agreement between the predicted and measured γ'' coarsening rate constants in
625 Table VI. Hence, it appears that such a high level of ΔG_{el} for the input dataset is
626 not appropriate in and of itself.

627 As suggested by an inspection of Equation (23), one modification to the
628 baseline input dataset that could offset the high level of ΔG_{el} does present itself,
629 however. Specifically, because ΔG_{el} and ΔG^* are of opposite sign, an increase in
630 the latter would tend to offset the high level of the former. In this regard,
631 Equations (20a) and (20b) reveal that a *reduction* in the thermodynamic factor
632 would increase ΔG^*. An analysis of the summary of thermodynamic factors in
633 Reference 70, and those for Nb in particular, suggests that the present value of
634 1.94 for this alloying element (Table III) is high, and that a value closer to 1.1
635 may be more appropriate. A simulation using a so-called modified baseline
636 dataset incorporating ΔG_{el} = 70 MPa, this lower value of the thermodynamic

637 factor of Nb, and a slightly higher value of $\sigma_{\gamma''-\gamma}$ (i.e., 62.3, rather 56, mJ/m^2)
638 gave predictions of the aging kinetics 973 K (red curve in Figure 2a) which
639 exhibited excellent agreement with the measurements of Han [52]. The predicted
640 average sizes of γ'' (30.7 nm) γ' (14.3 nm) were very similar to those from the
641 simulation with the baseline dataset (i.e., 28.1 nm and 14.3 nm, respectively).
642 Moreover, the change in the modified baseline input dataset of the
643 thermodynamic factor of niobium and the value of $\sigma_{\gamma''-\gamma}$ did not greatly affect
644 agreement between measured and predicted coarsening rate constants (Table
645 IX). The efficacy of this modified dataset was further supported by a comparison
646 of measured and predicted aging responses over a wide range of temperature,
647 which is discussed in a companion paper describing in-situ evaluations of
648 precipitation in superalloy 718 [72].

Table IX. Sensitivity Analysis for the Effect of the Niobium Thermodynamic Factor (TF) on the Coarsening Rate Constant, K (nm^3/s)*

Phase	Temp (K)	Nb TF	σ (mJ/m^2)	K (All Solutes)	K (RLS)	Measured K
γ''	943	1.94	56	0.0182	0.0293	0.0174
γ''	943	1.10	62.3	0.0225	0.0326	0.0174
γ''	973	1.94	56	0.0609	0.0981	0.083
γ''	973	1.10	62.3	0.0751	0.109	0.083
γ''	1003	1.94	56	0.213	0.341	0.229
γ''	1003	1.10	62.3	0.261	0.380	0.229
γ'	973	1.94	40	0.00150	0.00378	0.00261
γ'	973	1.10	40	0.00152	0.00378	0.00261
γ'	1023	1.94	40	0.00805	0.0201	0.0129
γ'	1023	1.10	40	0.00814	0.0201	0.0129

* K ≡ K_d (γ'') or K_r (γ'); RLS ≡ rate-limiting solute

3. *Diffusivities*

A number of simulations highlighted the effect of changes in the diffusivities controlling nucleation and subsequent growth for both γ'' (Nb and Cr) and γ' (Ti and Al) on kinetic predictions. The effect of increasing/decreasing the diffusivity on precipitation kinetics was straightforward for cases in which only the coefficient controlling growth, for example, was changed (e.g., Figures 5, 6). In particular, an increase/decrease in the diffusivity of chromium accelerated/retarded predicted precipitation kinetics (Figure 5a), resulted in larger/smaller γ'' sizes (Figure 5b), and led to a more/less rapid rise in the $f_{\gamma''}/f_{\gamma'}$ ratio (Figure 5c). The corresponding changes for similar levels of increase/decrease in the rate-limiting solute for growth of γ' (i.e., aluminum) were less noticeable, except for the predicted γ' sizes (Figure 6), largely because of the smaller volume fraction of this precipitate. Last, the trends were more complicated for simulations in which the diffusivities of the solutes that control both nucleation and growth were changed simultaneously. This complexity was illustrated for cases in which D_{Nb} and D_{Cr} were both doubled or halved (Figure 7) or D_{Ti} and D_{Al} were both doubled or halved (Figure 8).

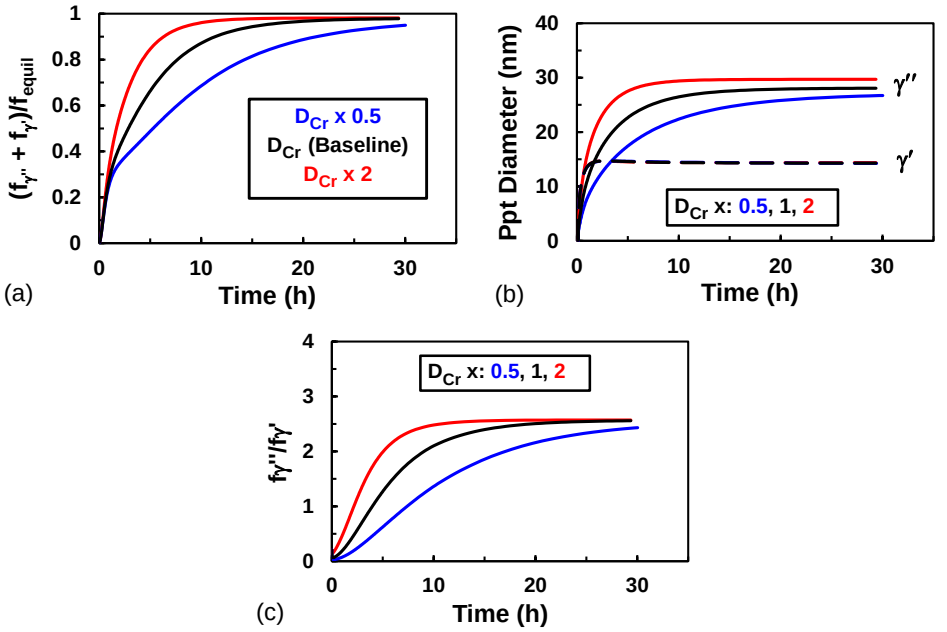

Figure 5. Fast-acting-simulation predictions of the effect of a two-fold variation in D_{Cr} on the temporal evolution of (a) the normalized total volume fraction, (b) precipitate diameters, and (c) ratio of the volume fractions of γ″ and γ′ during aging at 973 K.

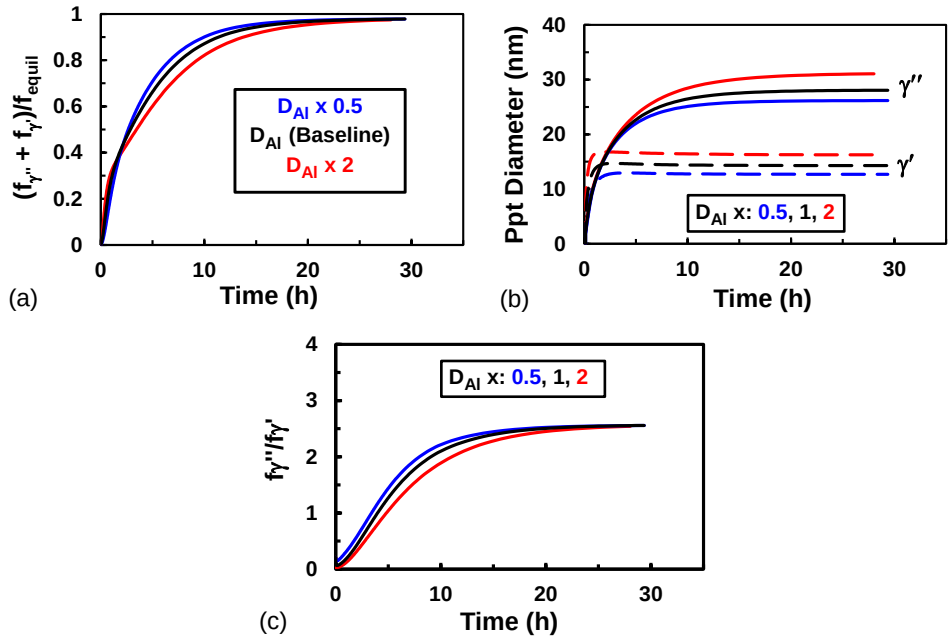

Figure 6. Fast-acting-simulation predictions of the effect of a two-fold variation in D_{Al} on the temporal evolution of (a) the normalized total volume fraction, (b) precipitate diameters, and (c) ratio of the volume fractions of γ″ and γ′ during aging at 973 K.

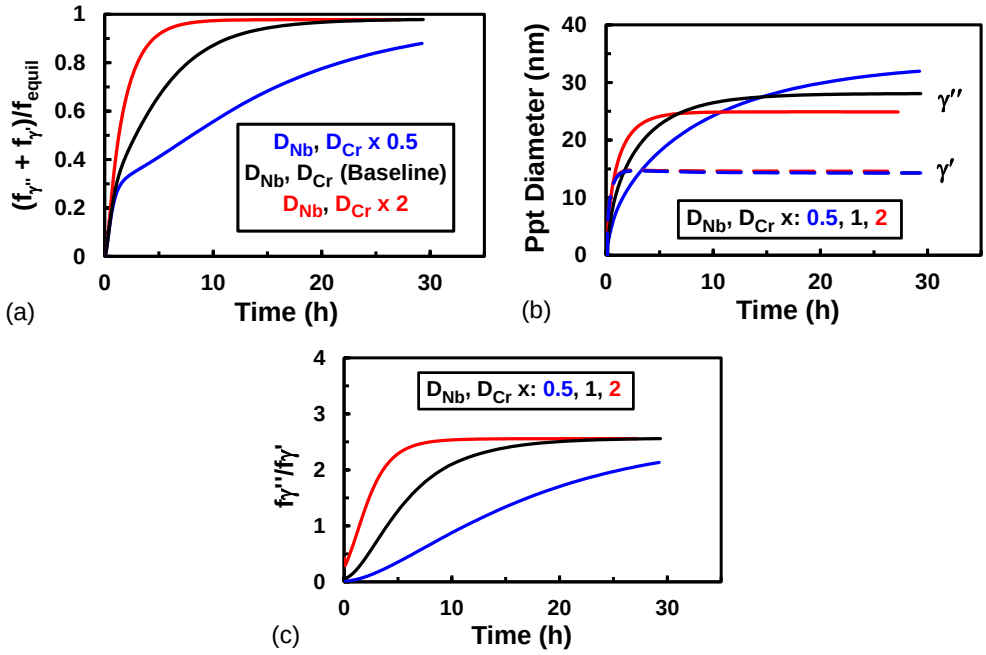

Figure 7. Fast-acting-simulation predictions of the effect of a two-fold variation in D_{Nb} and D_{Cr} on the temporal evolution of (a) the normalized total volume fraction, (b) precipitate diameters, and (c) ratio of the volume fractions of γ'' and γ' during aging at 973 K.

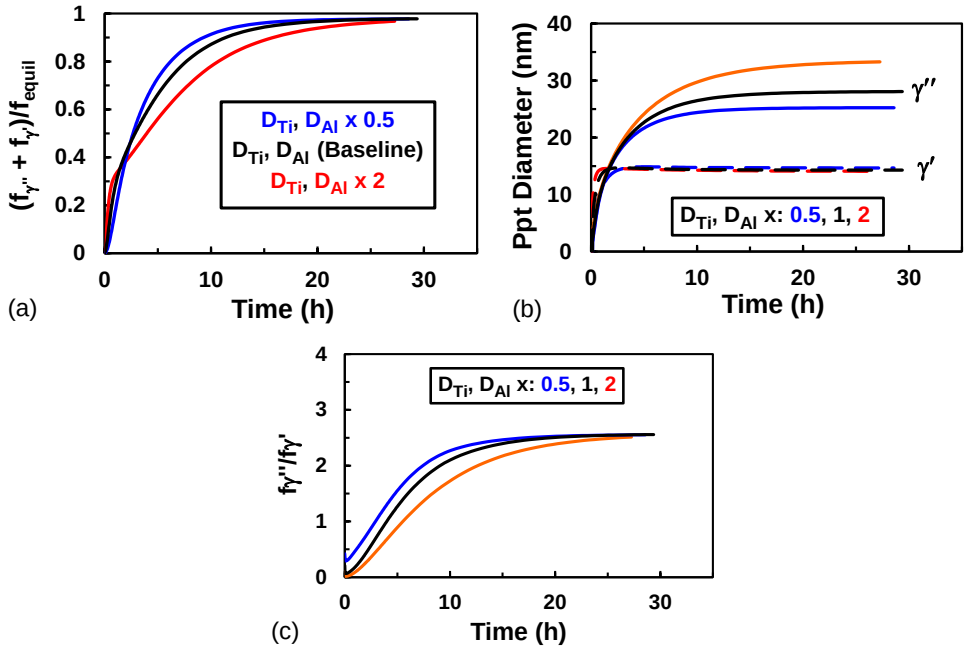

Figure 8. Fast-acting-simulation predictions of the effect of a two-fold variation in D_{Ti} and D_{Al} on the temporal evolution of (a) the normalized total volume fraction, (b) precipitate diameters, and (c) ratio of the volume fractions of γ'' and γ' during aging at 973 K.

V. FUTURE OUTLOOK

The present work has presented an initial attempt to develop a simple, engineering-oriented spreadsheet analysis for describing second-phase nucleation and growth for metallic systems with two precipitating phases such as superalloy 718 having γ'' and γ'. The approach appears to provide reasonable descriptions of precipitation kinetics and average sizes of the particles. More complete validation would be possible with further work to clarify the following:

- Phase equilibria/phase fractions as a function of temperature (and alloy composition).
- More accurate measurements of phase compositions as a function of alloy composition and temperature.
- Additional measurements of the off-diagonal diffusivity terms for ternary and higher-order systems of importance for quantifying the precipitation kinetics of 718.
- Additional work to verify the precise magnitudes of ΔG^* and ΔG_{el}.

VI. SUMMARY AND CONCLUSIONS

A fast-acting simulation approach to quantify the precipitation of γ'' and γ' in superalloy 718 was developed. The applicability of the analysis and corresponding input material properties were confirmed by replicating selected nucleation, growth, and coarsening observations in the literature. The key conclusions from this work are as follows:

687 (1) The processes of nucleation, growth, and coarsening of γ'' and γ'
688 precipitates are diffusion-controlled, each of whose kinetics can be quantified to a
689 first order using a single, rate-limiting solute.

690 (2) The nucleation of γ'' and γ' are driven by the partitioning of niobium and
691 titanium, respectively.

692 (3) The growth of disk-like/ellipsoidal γ'' and spheroidal γ' precipitates can
693 both be described using an exact solution to the one-dimensional diffusion
694 equation for the growth of an isolated spherical particle provided (1) the geometry
695 of γ'' is represented as a sphere with an effective radius that provides the same
696 growth rate as the corresponding disk/ellipsoid, and (2) the effect of soft
697 impingement of the concentration fields of adjacent particles is taken into
698 account. The rate-controlling solute appears to be chromium or aluminum for γ''
699 and γ', respectively.

700 (4) The coarsening of both γ'' and γ' are described by classical LSW
701 theory modified to account for the composition, (finite) volume fraction, and
702 shape of each phase, the composition of the γ matrix, and the thermodynamic
703 factors of solutes in the matrix. Predicted rate constants based on all solutes or a
704 single rate-limiting solute bound experimental observations in the literature.

705 *Acknowledgements* – Major portions of this work were conducted as part of the
706 in-house research of the Air Force Research Laboratory's Materials and
707 Manufacturing Directorate. Encouragement from and discussions with W. Cao,
708 T.P. Gabb, T.A. Parthasarathy, D.F. Paulonis, and R.A. Thomas are very much
709 appreciated.

List of Symbols

A	ratio of length of major to minor axis of oblate ellipsoidal γ'' precipitate
A_{czh}	diffusivity at 1423 K per Ref. 62
a_o	lattice parameter
C	composition (atomic fraction)
C_γ, $C_{\gamma''}$, $C_{\gamma'}$	equilibrium solute concentration in the γ matrix and γ''/γ' precipitates
D	diffusivity
D_{eff}	effective diffusivity
f	volume fraction
J	nucleation rate
J_o	steady-state nucleation rate
K_{MLSW}	volume-fraction modified LSW coarsening-rate constant
k_B	Boltzmann's constant
K_{β^*}, K_Z, $K_{\Delta G^*}$	ratios of the frequency factor, Zeldovich nonequilibrium factor, and ΔG^* for specific non-spherical nuclei relative to those for a spherical nucleus
q	ratio of thickness-to-diameter of disk-like γ'' precipitate
r	precipitate radius
r_{eff}	effective radius of an equivalent sphere for an ellipsoidal γ'' precipitate
r^*	critical radius of disk or spherical precipitate
R	universal gas constant
T	absolute temperature
t	time
V_M	molar volume
v	activity coefficient
V	precipitate volume
w	volume-fraction function (in relation for coarsening rate constant)
ΔG^*	volumetric (chemical) free energy of transformation
ΔG_p	elastic (misfit) energy
ΔH	enthalpy of formation of γ'
ΔS	entropy of formation of γ'
β	growth-rate parameter for oblate ellipsoidal precipitates
λ^2	growth-rate parameter for oblate spherical precipitates
Ω	supersaturation
$\sigma_{\gamma''\text{-}\gamma}$, $\sigma_{\gamma'\text{-}\gamma}$	precipitate-matrix interface energies
δ	tetragonal distortion along c axis of γ'' precipitates
Δ	uniform dilational strain for of γ'' precipitates
μ	shear modulus
υ	Poisson's ratio
τ	incubation time constant

References

1. M. J. Donachie (ed.): *Superalloys: Source Book*, ASM International, Materials Park, OH, 1984.
2. *Proc. 13th Inter. Symp. on Superalloys*, M. Hardy, E. Huron, U. Glatzel, B. Griffin, B. Lewis, C. Rae, V. Seetharaman, and S. Tin, eds., TMS, Warrendale, PA, 2016.
3. *Proc. 9th Inter. Symposium on Superalloy 718 and Derivatives*, E. Ott, X. Liu, J. Andersson, Z. Bi, K. Bockenstedt, I. Dempster, J. Groh, K. Heck, P. Jablonski, M. Kaplan, D. Nagahama, and C. Sudbrack, eds., 2018, TMS, Pittsburgh, PA, 2018.
4. D. Paulonis and J.J. Schirra: in *Superalloys 718, 625, 706, and Various Derivatives*, E.A. Loria, ed., TMS, Warrendale, PA, 2001, pp. 13-23.
5. R.E. Schafrik, D.D. Ward, and J.R. Groh: in *Superalloys 718, 625, 706, and Various Derivatives*, E.A. Loria, ed., TMS, Warrendale, PA, 2001, pp. 1-11.
6. J.W. Brooks and P.J. Bridges: in *Superalloys 1988*, S. Reichman, D.N. Duhl, G. Mauer, S. Antolovich, and C. Lund, eds., TMS, Warrendale, PA, 1988, pp. 33-42.
7. A. Oradei-Basile and J.F. Radovich: in *Superalloys 718, 625, and Various Derivatives*, E.A. Loria, ed., TMS, Warrendale, PA, 1991, pp. 325-335.
8. C.I. Garcia, D.E. Camus, E.A. Loria, and A.J. DeArdo: in *Superalloys 718, 625, and Various Derivatives*, E.A. Loria, ed., TMS, Warrendale, PA, 1991, pp. 925-941.

9. C.I. Garcia, A.K. Lis, E.A. Loria, and A.J. DeArdo: in *Superalloys 1992*, S.D. Antolovich, R.W. Stusrud, R.A. MacKay, D.L. Anton, T. Khan, R.D. Kissinger, and D.L. Klarstrom, eds., TMS, Warrendale, PA, 1992, pp. 527-536.
10. H. Chandler: *Heat Treater's Guide: Practices and Procedures for Nonferrous Alloys*, ASM International, Materials Park, OH, 1996.
11. C. Slama and G. Cizeron: Etude du Comportement Structural de l'Alliage NC 19 Fe Nb (Inconel 718), *J. de Physique III*, 1997, vol. 7, pp. 665-688.
12. A. Thomas, M. El-Wahabi, J.M. Cabrera, and J.M. Prado: *J. Mater. Proc. Technol.*, vol. 177, 2006, pp. 469-472.
13. R. Cozar and P. Pineau: *Metall. Trans.*, 1973, vol. 4, pp. 47-59.
14. M. Sundararaman, P. Mukhopadhyay, and S. Banerjee: *Metall. Trans. A*, 1992, vol. 23A, pp. 2015-2028.
15. R.D. Doherty: in *Physical Metallurgy*, R.W. Cahn and P. Haasen, eds., North-Holland, Amsterdam, 1996, ch. 15.
16. T.P. Gabb, D.G. Backman, D.Y. Wei, D.P. Mourer, D.U. Furrer, A. Garg, and D.L. Ellis: in *Superalloys 2000*, T.M. Pollock, R.D. Kissinger, R.R. Bowman, K.A. Green, M. McLean, S. Olson, and J.J. Schirra, eds., TMS, Warrendale, PA, 2000, pp. 405-414.
17. H.J. Jou, P.W. Voorhees, and G.B. Olson: in *Superalloys 2004*, K.A. Green, T.M. Pollock, H. Harada, T.E. Howson, R.C. Reed, J.J. Schirra, and S. Walston, eds, TMS, Warrendale, PA, 2004, pp. 877-886.

18. G.B. Olson, H.J. Jou, J. Jung, J.T. Sebastian, A. Misra, I. Locci, and D. Hull: in *Superalloys 2008*, R.C. Reed, K.A. Green, P. Caron, T.P. Gabb, M.G. Fahrmann, E.S. Huron, and S.A. Woodard, eds., TMS, Warrendale, PA, 2008, pp. 923-932.
19. R. Radis, M. Schaffer, M. Albu, G. Kothleitner, P. Polt, and E. Kozeschnik: *Acta Mater.*, 2009, vol. 57, pp. 5739-5747.
20. B. Wang, F. Zhang, W. Cao, S. Chen, and S. Kou: *Metall. Mater. Trans. A*, 2015, vol. 46A, pp. 115-122.
21. S.L. Semiatin, S-L. Kim, F. Zhang, and J.S. Tiley: *Metall. Mater. Trans. A*, 2015, vol. 46A, pp. 1715-1730.
22. S.L. Semiatin, N.C. Levkulich, and J.S. Tiley: *Metall. Mater. Trans. A*, 2019, vol. 50A, pp. 5281-5296.
23. M.J. Anderson, F. Schulz, Y. Lu, H. Kitaguchi, P. Bowen, C. Argyrakis, and H.C. Basoalto: *Acta Mater.*, 2020, vol. 161, pp. 81-100.
24. J.P. Simmons, C. Shen, and Y. Wang: *Scripta Mater.*, 2000, pp. 935-942.
25. Y.H. Wen, J.P. Simmons, C. Shen, C. Woodward, and Y. Wang: *Acta Mater.*, 2003, vol. 51, pp. 1123-1132.
26. M. Fleck, F. Schleifer, M. Holzinger, and U. Glatzel: *Metall. Mater. Trans. A*, 2018, vol. 49A, pp. 4146-4157.
27. I.J. Moore, M.G. Burke, and E.J. Palmiere: *Acta Mater.*, 2016, vol. 119, pp. 157-166.
28. R. Radis, G.A. Zickler, M. Stockinger, C. Sommitsch, and E. Kozeschnik: in *Proc. 7th International Sympsium on Superalloy 718 and Derivatives*, E.A.

Ott, J.R. Groh, A. Banik, I. Dempster, T.P. Gabb, R. Helmink, X. Liu, A. Mitchell, G.P. Sjoberg, and A. Wusatowski-Sarnek, eds. TMS, Warrendale, PA, 2010, pp. 569-578.

29. K. Wu, F. Zhang, S. Chen, W. Cao, and Y.A. Chang: : in *Superalloys 2008*, R.C. Reed, K.A. Green, P. Caron, T.P. Gabb, M.G. Fahrmann, E.S. Huron, and S.A. Woodard, eds., TMS, Warrendale, PA, 2008, pp. 933-939.
30. F. Zhang, W. Cao, C. Zhang, S. Chen, J. Zhu, and D. Lv; in *Proceedings, 9th International Symposium on Superalloy 718 & Derivatives: Energy, Aerospace, and Industrial Applications*, E. Ott, ed., TMS, Pittsburgh, 2018, pp. 147-161.
31. A. Drexler, B. Oberwinkler, S. Primig, C. Turk, E. Povoden-Karadeniz, A. Heinemann, W. Ecker, and M. Stockinger: *Mater. Sci. Eng. A*, 2018, vol. A723, pp. 314-323.
32. Z.K. Low, T. Chaise, D. Bardel, S. Cazottes, P. Chaudet, M. Perez, and D. Nelias: *Acta Mater.*, 2018, vol. 156, pp. 31-42.
33. H.I. Aaronson and F.K. LeGoues: *Metall. Trans. A*, 1992, vol. 23, pp. 1915-1945.
34. S.Q. Xiao and P. Haasen: *Acta Metall. et Mater.*, 1991, vol. 39, pp. 651-659.
35. J.W. Christian: *Acta Metall.*, 1958, vol. 6, pp. 377-379.
36. K.S. Chan, J.K. Lee, G.J. Shiflet, K.C. Russell, and H.I. Aaronson: *Metall. Trans. A*, 1978, vol. 9A, pp. 1016-1017.
37. L. Kampmann and M. Kahlweit: *Berichte der Bunsen-Gesellschaft Physikalische Chemie*, 1970, vol. 94, pp. 456-462.

38. H.S. Carslaw and J.C. Jaeger: *Conduction of Heat in Solids*, Oxford University Press, London, 1959.

39. H.B. Aaron, D. Fainstein, and G.R. Kotler: *J. Appl. Physics*, 1970, vol. 41, pp. 4404-4410.

40. O. Grong and H.R. Shercliff: *Progress in Materials Science*, 2002, vol. 47, pp. 163-282.

41. F.S. Ham: *J. Phys. Chem. Solids*, 1958, vol. 6, pp. 335-351.

42. F.S. Ham: *Q. Appl. Math.*, 1959, vol. 17, pp. 137-145.

43. G. Horvay and J.W. Cahn: *Acta Metall.*, 1961, vol. 9, pp. 695-705.

44. M. Ferrante and R.D. Doherty: *Acta Metall.*, 1979, vol. 27, pp. 1603-1614.

45. S.L. Semiatin, T.M. Lehner, J.D. Miller, R.D. Doherty, and D.U. Furrer: *Metall. Mater. Trans. A*, 2007, vol. 38A, pp. 910-921.

46. I.M. Lifshitz and V.V. Slyozov: *J. Phys. Chem. Solids*, 1961, vol. 19, pp. 35-51.

47. C. Wagner: *Zeit. Elektrochem.*, 1961, vol. 65, pp. 581-591.

48. H. A. Calderon, P.W. Voorhees, J.L. Murray, and G. Kostorz: *Acta Metall. et Mater.*, 1994, vol. 42, pp. 991-1000.

49. P.W. Voorhees and M.E. Glicksman: *Acta Metall.*, 1984, vol. 32, pp. 2013-2030.

50. J.D. Boyd and R.B. Nicholson: *Acta Metall.*, 1971, vol. 19, pp. 1379-1391.

51. C.J. Kuehmann and P.W. Voorhees: *Metall. and Mater. Trans A*, 1996, vol. 27A, pp. 937-943.

52. Y.F. Han: M.S. Thesis, University of Manitoba, Winnipeg, Canada, 1981.

53. Y.F. Han, P. Deb, M.C. Chaturvedi: *Metal Sci.*, 1983, vol, 16, pp. 555-561.

54. R.B. Li, M. Yao, W.C. Liu, and X.C. He: *Scripta Mater.*, 2002, vol. 46, pp. 635-638.

55. X. Xie, J. Dong, G. Wang, and W You: in *Superalloys 718, 625, 706, and Derivatives*, E.A. Loria, ed., TMS, Warrendale, PA, 2005, pp. 287-298.

56. T.M. Smith, N.M. Senanayake, C.K. Sudbrack, P. Bonacuse, R.B. Rogers, P. Chao, and J. Carter: *Mater. Characterization*, 2019, vol. 148, pp. 178

57. R.Y. Zhang, H.L. Qin, Z.N. Bi, J. Li, S. Paul, T.L. Lee, B. Nenchev, J. Zhang, S. Kabra, J.F. Kelleher, and H.B. Dong: *Metall. Mater. Trans. A*, 2019, vol. 50A, pp. 5421-5432.

58. R. Lawitzki, S. Hassan, L. Karge J. Wagner, D. Wang, J. von Kobylinski, C. Krempaszky, M. Hofmann, R. Gilles, and G. Schmitz: *Acta Mater.*, 2019, vol. 163, pp. 28-39.

59. M.K. Miller, S.S. Babu, and M.G. Burke: *Mater. Sci. Eng. A*, 2002, vol. A327, pp. 84-88.

60. A. Devaux, L. Naze, R. Molins, A. Pineau, A. Organista, J.Y. Guedou, J.F. Uginet, and P. Heritier: *Mater. Sci. Eng. A*, 2008, vol. A486, pp. 117-122.

61. R.Y. Zhang, H.L. Qin, Z.N. Bi, J. Li, S. Paul, T.L. Lee, S.Y. Zhang, J. Zhang, and H.B. Dong: *Metall. Mater. Trans. A*, 2020, vol. 51A, pp. 1860-1873.

62. C.E. Campbell, J.C. Zhao, and M.F. Henry: *J. Phase Equilibria and Diffusion*, 2004, vol. 25, pp. 6-15.

63. M.S.A. Karunaratne, D.C. Cox, P. Carter, and R.C. Reed RC: in *Superalloys 2000*, T.M. Pollock, R.D. Kissinger, R.R. Bowman, K.A. Green, M. McLean, S. Olson, and J.J. Schirra, eds., TMS, Warrendale, PA, 2000, pp. 263-272.

64. S.L. Semiatin, N.C. Levkulich, A.R.C. Gerlt, E.J. Payton, J.S. Tiley, F. Zhang, R.A. MacKay, R.V. Miner, and T.P. Gabb: *Metall. Mater. Trans. A*, 2019, vol. 50A, pp. 2289-2301.

65. M. Dayananda: *Mater. Sci. Eng. A*, 1989, vol. A121, pp. 351-359.

66. G. Xu, Y. Liu, and Z. Kang: *Metall. Mater. Trans. B*, 2016, vol. 47B, pp. 3126-3133.

67. J.A. Nesbitt and R.W. Heckel: *Metall. Trans. A*, 1987, vol. 18A, pp. 2061-2073.

68. K. Kulkarni, G.P.S. Chauhan: *AIP Advances*, 2015, vol. 5 (097162), pp. 1-7.

69. C.K. Sudbrack, R.D. Noebe, D.N. Seidman: *Acta Mater*. 2007, vol. 55, pp. 119-130.

70. S.L. Semiatin, F. Zhang, R. Larsen, L.A. Chapman, and D.U. Furrer: *Integrating Mater. Mfg. Innovation*, 2016, vol. 5, no. 3, pp. 1-20.

71. R. Wagner and R. Kampmann: in *Materials Science and Technology*, Vol. 5, P. Haasen, ed., VCH, Weinheim, Germany, 1991, pp. 213-303.

72. J. Cormier, P. Gadaud, M. Czaplicki, R.Y. Zhang, H.B. Dong, T.M. Smith, F. Zhang, J.S. Tiley, and S.L. Semiatin: Paper submitted to *Metall. Mater. Trans. A*, 2020.

Table I. Nucleation Rate Factors for Non-Spherical Nuclei

Factor	Disk q = 0.5	Ellipsoid q = 0.5	Disk q = 0.333	Ellipsoid q = 0.333
$K_{\Delta G^*}$	0.75	0.688	0.5	0.481
K_{β^*}	1	0.875	0.833	0.778
K_Z	1.155	1.206	1.414	1.441
$K_{\beta^*} \times K_Z$	1.155	1.055	1.179	1.121

Table II. Compositions Used in the Present Work

Material	Fe	Cr	Mo	Nb	Ti	Al	Ni
Overall (w/o)	20.7	18	3	5.3	0.97	0.57	Bal
Overall (a/o)	21.5	20	1.76	3.31	1.18	1.24	Bal
γ'' (a/o)	1.9	2.18	2.0	18.5	4.3	1.2	Bal
γ' (a/o)	2.3	1.95	1.1	7.38	7.86	8.95	Bal

Table III. Values of the Thermodynamic Factors (TF) and ΔG^*

Element	TF	γ'' ΔG^* (J/mol)	γ' ΔG^* (J/mol)
Fe	0.82	399	392
Cr	0.91	317	3
Mo	0.92	~0	~0
Nb	1.94	756	271
Ti	1.30	219	423
Al	1.25	8	176

Table IV. Experimentally-Fitted Effective Diffusivity of Solutes in Alloy 718 at 1423 K (1150 °C) [62]

Element	Diffusivity (m^2/s)
Fe	1.56×10^{-14}
Cr	1.58×10^{-14}
Mo	1.66×10^{-14}
Nb	6.69×10^{-14}
Ti	2.02×10^{-14}
Al	1.36×10^{-14}

Table V. Predicted Values of the Coarsening Rate Constant K_d (in nm^3/s) for γ'' as a Function of Temperature*

Element	943 K	973 K	1003 K
Fe	0.176	0.588	2.04
Cr	0.183	0.612	2.13
Mo	14.6	48.9	169.3
Nb	0.0421	0.141	0.498
Ti	0.0739	0.247	0.866
Al	31.6	105.7	370.7
All Solutes	**0.0206**	**0.0689**	**0.242**
Measurement [60]	**0.0174**	**0.083**	**0.229**

* All diffusivities multiplied by a factor of 0.625; σ = 56 mJ/m^2, q = 0.45 (943 K), 0.40 (973 K), or 0.32 (1003 K)

Table VI. Predicted Values of the Coarsening Rate Constant K_d (in nm^3/s) for γ'' as a Function of Temperature*

Element	943 K	973 K	1003 K
Fe	0.281	0.940	3.27
Cr	**0.0293**	**0.0981**	**0.341**
Mo	23.4	78.3	270.9
Nb	0.0805	0.269	0.951
Ti	0.211	0.707	2.48
Al	50.6	169.2	593.1
All Solutes	**0.0182**	**0.0609**	**0.213**
Measurement [60]	**0.0174**	**0.083**	**0.229**

* Chromium diffusivity multiplied by a factor of 0.1; σ = 56 mJ/m^2, q = 0.45 (943 K), 0.40 (973 K), or 0.32 (1003 K)

Table VII. Predicted Values of the Coarsening Rate Constant K_r (in nm^3/s) for γ' as a Function of Temperature*

Element	973 K	1023 K
Fe	0.0362	0.193
Cr	**0.00378**	**0.0201**
Mo	2.98	15.8
Nb	0.0572	0.313
Ti	0.00388	0.0209
Al	0.0102	0.0552
All Solutes	**0.00150**	**0.00805**
Measurement [52]	**0.00261**	**0.0129**

* Chromium diffusivity multiplied by a factor of 0.1, σ = 40 mJ/m^2.

Table VIII. Sensitivity Analysis for ΔG_{el}

ΔG_{el} (MPa)	$\sigma\gamma''$-γ (mJ/m^2)	γ'' Diameter (nm)	γ'' Diameter (nm)
12	56.0	28.1	14.3
17	53.8	31.9	14.3
25.5	49.8	32.6	14.3
70	25.3	44.6	14.3

Table IX. Sensitivity Analysis for the Effect of the Niobium Thermodynamic Factor (TF) on the Coarsening Rate Constant, K (nm^3/s)*

Phase	Temp (K)	Nb TF	σ (mJ/m^2)	K (All Solutes)	K (RLS)	Measured K
γ''	943	1.94	56	0.0182	0.0293	0.0174
γ''	943	1.10	62.3	0.0225	0.0326	0.0174
γ''	973	1.94	56	0.0609	0.0981	0.083
γ''	973	1.10	62.3	0.0751	0.109	0.083
γ''	1003	1.94	56	0.213	0.341	0.229
γ''	1003	1.10	62.3	0.261	0.380	0.229
γ'	973	1.94	40	0.00150	0.00378	0.00261
γ'	973	1.10	40	0.00152	0.00378	0.00261
γ'	1023	1.94	40	0.00805	0.0201	0.0129
γ'	1023	1.10	40	0.00814	0.0201	0.0129

* $K \equiv K_d$ (γ'') or K_r (γ'); RLS $\equiv$ rate-limiting solute

Figure Captions

Figure 1. Equilibrium fractions of the γ'' and γ' phases as a function of temperature.

Figure 2. Fast-acting-simulation predictions of the temporal evolution of (a) the normalized total volume fraction, (b) precipitate diameters, and (c) ratio of the volume fractions of γ'' and γ' during aging at 973 K. Simulation predictions correspond to the baseline (black curves) or modified-baseline (red curves) input datasets. The predictions in (a) are compared to measurements by Han [52] (data points).

Figure 3. Fast-acting-simulation predictions of the effect of a $\pm$1.5 mJ/m^2 variation in $\sigma_{\gamma''\text{-}\gamma}$ on the temporal evolution of (a) the normalized total volume fraction, (b) precipitate diameters, and (c) ratio of the volume fractions of γ'' and γ' during aging at 973 K.

Figure 4. Fast-acting-simulation predictions of the effect of a $\pm$1.5 mJ/m^2 variation in $\sigma_{\gamma'\text{-}\gamma}$ on the temporal evolution of (a) the normalized total volume fraction, (b) precipitate diameters, and (c) ratio of the volume fractions of γ'' and γ' during aging at 973 K.

Figure 5. Fast-acting-simulation predictions of the effect of a two-fold variation in D_{Cr} on the temporal evolution of (a) the normalized total volume fraction, (b) precipitate diameters, and (c) ratio of the volume fractions of γ'' and γ' during aging at 973 K.

Figure 6. Fast-acting-simulation predictions of the effect of a two-fold variation in D_{Al} on the temporal evolution of (a) the normalized total volume

fraction, (b) precipitate diameters, and (c) ratio of the volume fractions of γ'' and γ' during aging at 973 K.

Figure 7. Fast-acting-simulation predictions of the effect of a two-fold variation in D_{Nb} and D_{Cr} on the temporal evolution of (a) the normalized total volume fraction, (b) precipitate diameters, and (c) ratio of the volume fractions of γ'' and γ' during aging at 973 K.

Figure 8. Fast-acting-simulation predictions of the effect of a two-fold variation in D_{Ti} and D_{Al} on the temporal evolution of (a) the normalized total volume fraction, (b) precipitate diameters, and (c) ratio of the volume fractions of γ'' and γ' during aging at 973 K.